

# SR<sup>2</sup>-Net: A General Plug-and-Play Model for Spectral Refinement in Hyperspectral Image Super-Resolution

Ji-Xuan He<sup>1,2\*</sup>, Guohang Zhuang<sup>2\*</sup>, Junge Bo<sup>1†</sup>, Tingyi Li<sup>1</sup>, Chen Ling<sup>1</sup>, Yanan Qiao<sup>1‡</sup>

<sup>1</sup>School of Computer Science and Technology, Xi'an Jiaotong University

<sup>2</sup>School of Computer Science and Information Engineering, Hefei University of Technology

## Abstract

HSI-SR aims to enhance spatial resolution while preserving spectrally faithful and physically plausible characteristics. Recent methods have achieved great progress by leveraging spatial correlations to enhance spatial resolution. However, these methods often neglect spectral consistency across bands, leading to spurious oscillations and physically implausible artifacts. While spectral consistency can be addressed by designing the network architecture, it results in a loss of generality and flexibility. To address this issue, we propose a lightweight plug-and-play rectifier, physically priors Spectral Rectification Super-Resolution Network (**SR<sup>2</sup>-Net**), which can be attached to a wide range of HSI-SR models without modifying their architectures. **SR<sup>2</sup>-Net** follows an *enhance-then-rectify* pipeline consisting of (i) Hierarchical Spectral-Spatial Synergy Attention (**H-S<sup>3</sup>A**) to reinforce cross-band interactions and (ii) Manifold Consistency Rectification (**MCR**) to constrain the reconstructed spectra to a compact, physically plausible spectral manifold. In addition, we introduce a degradation-consistency loss to enforce data fidelity by encouraging the degraded SR output to match the observed low resolution input. Extensive experiments on multiple benchmarks and diverse backbones demonstrate consistent improvements in spectral fidelity and overall reconstruction quality with negligible computational overhead. Our code will be released upon publication.

## 1 Introduction

Hyperspectral image (HSI) captures dense spectral information at each spatial location, typically spanning tens to hundreds of spectral bands. It has been applied to numerous areas such as remote sensing [Aburaed *et al.*, 2023; Gao *et al.*, 2025], agriculture [Wang *et al.*, 2021], industrial inspection [Yang *et al.*, 2025], and biomedical imaging [Kotwal *et al.*, 2025]. However, due to limitations in imaging

\*Equal contribution. Email: jixuanhe@mail.hfut.edu.cn

†Corresponding author.

‡Corresponding author.

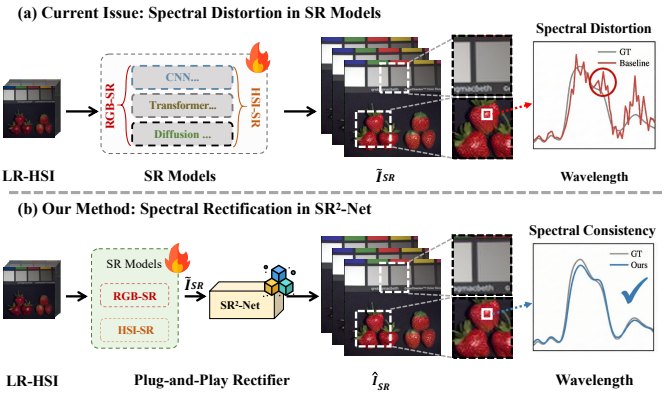


Figure 1: Motivation of **SR<sup>2</sup>-Net**. (a) General SR models tend to introduce spectral distortion during reconstruction. (b) Spectral consistency is achieved via the plug-and-play **SR<sup>2</sup>-Net** rectifier.

hardware, achieving high spectral and spatial resolution simultaneously remains a significant challenge. A common approach is to preserve high spectral resolution at the expense of spatial resolution. Therefore, to compensate for the lack of spatial details, it becomes particularly necessary to develop hyperspectral image super-resolution reconstruction techniques.

In recent years, RGB image super-resolution (SR) has advanced rapidly and has become a relatively mature research area. With effective designs for spatial detail restoration, these methods perform remarkably well in natural image reconstruction and have led to the development of a large number of high-performance models [Zhang *et al.*, 2018b; Liang *et al.*, 2021; Chen *et al.*, 2023]. Inspired by this success, it may seem straightforward to transfer RGB-SR designs to HSI-SR. However, this transfer remains far from trivial. HSI exhibits high-dimensional spectral structures with strong cross-band correlations, which requires reconstructed results to be reliable in both spatial and spectral domains. In contrast, most RGB-SR models are designed for three-channel inputs and primarily focus on spatial texture recovery, while lacking explicit modeling of multi-band constraints. So, directly applying RGB-SR models to HSI-SR still faces significant challenges.

Nevertheless, researchers have increasingly focused on HSI-SR and have proposed various HSI-specific models that exploit spectral and spatial correlations to improve recon-

struction quality [Wu *et al.*, 2024; Fu *et al.*, 2016]. In addition, interaction mechanisms have been incorporated to model spectral and spatial dependencies [Zheng *et al.*, 2021; Zhang *et al.*, 2025]. However, owing to insufficient modeling of cross-band relationships and the lack of explicit constraints on spectral structure, existing methods may still suffer from spectral shifts and cross-band inconsistencies during reconstruction.

Based on the above observations, we further extend our focus from spatial reconstruction quality to spectral reliability. As shown in Fig. 1, existing SR methods can often produce visually plausible spatial details, but they may introduce non-physical spectral oscillations in the reconstructed spectra. In real scenes, spectral variations with respect to wavelength are generally smooth and continuous. Therefore, such oscillations are physically implausible and can distort the spectral curve shape as well as key absorption characteristics. This spectral bias weakens the stability and distinguishability of hyperspectral features, which can lead to more false alarms and increased class confusion in downstream tasks such as classification and detection [He *et al.*, 2024; Wang *et al.*, 2024].

To address these limitations, we propose *SR<sup>2</sup>-Net*, a lightweight plug-and-play rectifier with physically priors spectral for HSI-SR. *SR<sup>2</sup>-Net* can be appended to the output of any SR model and trained end-to-end without modifying the SR architecture. It follows an enhance-then-rectify strategy: an enhancement stage (H-S<sup>3</sup>A) promotes stable interactions along the spectral axis, and a rectification stage (MCR) calibrates the reconstruction toward physically plausible spectral structures to suppress non-physical spectral artifacts. We also introduce a degradation-consistency loss to enforce that the reconstructed HR image aligns with the LR observation after degradation, ensuring data fidelity between the two.

**Our contributions are summarized as follows:**

- We introduce *SR<sup>2</sup>-Net*, a lightweight plug-and-play rectifier with physical priors for hyperspectral super-resolution. It improves spectral fidelity without modifying backbone architectures.
- We present an enhance-then-rectify refinement. H-S<sup>3</sup>A promotes stable cross-band interaction, while MCR calibrates reconstructions toward manifold-consistent spectra to suppress non-physical spectral artifacts. A self-supervised cycle constraint is used during training to enforce degradation consistency.
- We test *SR<sup>2</sup>-Net* with a broad set of SR backbones, including generic and HSI-specific CNN/Transformer models and a diffusion-based HSI-SR method. The results show improved spectral fidelity and overall reconstruction quality with minimal extra cost.

## 2 Related Work

### 2.1 Image Super-Resolution

Image super-resolution (SR) aims to reconstruct low-resolution images into high-resolution images. In recent

years, SR technology has developed rapidly, and the introduction of deep learning architectures has significantly improved spatial detail recovery capabilities and perceptual quality. CNN-based methods typically enhance local representation capabilities through deep residual learning and attention mechanisms, with RCAN [Zhang *et al.*, 2018b] being a representative baseline model. Transformer-based SR methods leverage self-attention mechanisms to strengthen long-range dependency modeling, and SwinIR [Liang *et al.*, 2021] and subsequent models (*e.g.* HAT [Chen *et al.*, 2023]) have become widely adopted backbone networks in image restoration tasks. Recently, state-space models have been introduced into the field of image restoration due to their efficient modeling and computational advantages, such as VMamba [Liu *et al.*, 2024] and MambaIR [Guo *et al.*, 2024]. In addition, the application of diffusion models in SR and blind restoration has also attracted attention. ResShift [Yue *et al.*, 2023] and DiffBIR [Lin *et al.*, 2023] demonstrate that iterative generation can restore sharper high-frequency details, but artifact suppression and stability control remain open problems. Therefore, these advances have produced strong and reusable SR backbones, which makes it appealing to reuse mature models rather than redesigning architectures for each new modality.

### 2.2 Hyperspectral Image Super-Resolution

Unlike SR of RGB images, hyperspectral image super-resolution (HSI-SR) is geared towards the reconstruction of multi-band (multi-channel) data. The channel dimension of a hyperspectral image forms an ordered spectral sequence in which adjacent bands are densely sampled and highly correlated. As a result, HSI-SR must not only recover spatial structures but also preserve physically meaningful spectral characteristics. Spectral distortion can severely degrade the reliability of subsequent analysis. Existing deep learning based HSI-SR methods generally follow two main directions. One direction trains generic SR backbones on hyperspectral cubes by treating spectral bands as channels. This strategy benefits from mature architectures and strong spatial reconstruction capability and commonly adopts RCAN [Zhang *et al.*, 2018b] and SwinIR [Liang *et al.*, 2021] as baseline models. The other focuses on designing architectures specifically tailored for HSI by explicitly modeling spectral and spatial coupling, as exemplified by SSPSR [Jiang *et al.*, 2020] and ESSAformer [Zhang *et al.*, 2023]. In addition, diffusion-based approaches have also been explored for hyperspectral image restoration and super-resolution. Recent representative works include DDS2M [Miao *et al.*, 2023] and HIR-Diff [Pang *et al.*, 2024].

Despite these advances, many existing methods still suffer from limited fidelity. The reconstructed images may appear spatially sharp but remain spectrally unreliable, often exhibiting cross-band distortions or spurious oscillations. We propose a lightweight and plug-and-play spectral corrector that can be attached to both generic super-resolution models and HSI-specific variants. This design improves spectral fidelity without altering the original network architecture.

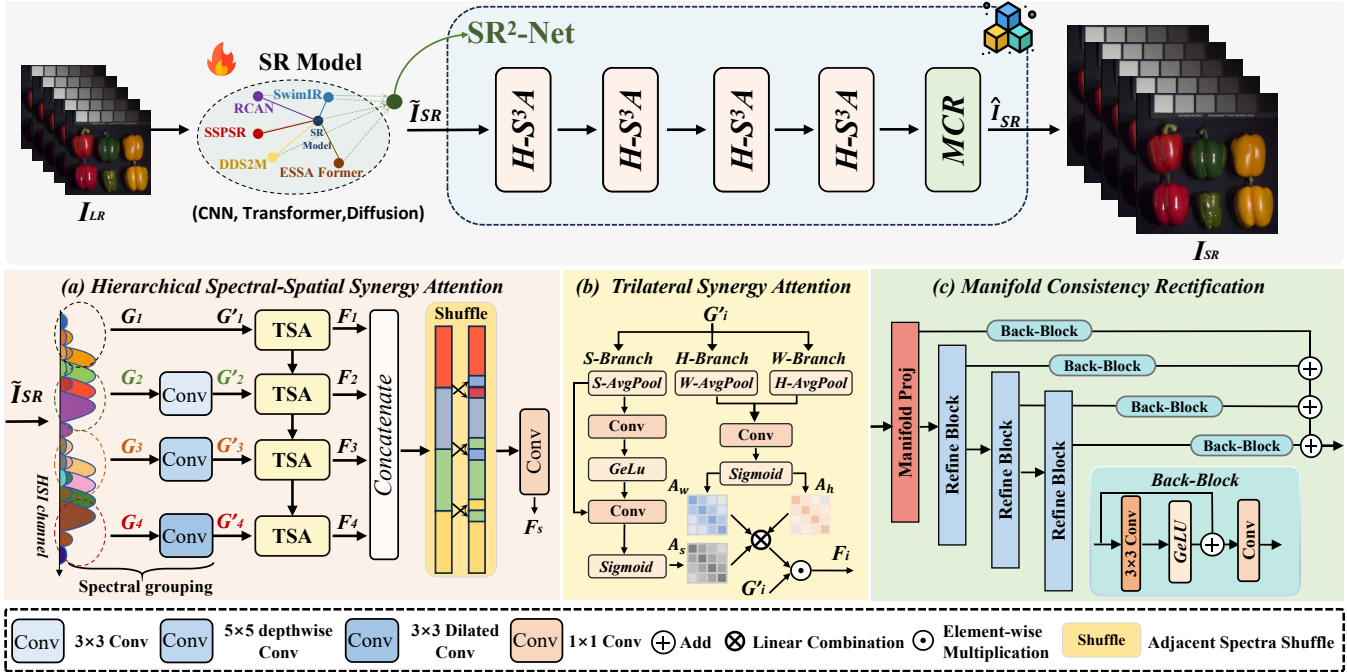


Figure 2: The overview of  $SR^2$ -Net, a plug-and-play rectifier for hyperspectral image super-resolution. Given an LR input  $I_{LR}$ , an SR model produces an initial reconstruction  $\tilde{I}_{SR}$ , which is then refined by  $SR^2$ -Net to obtain the rectified output  $\hat{I}_{SR}$ . (a) H-S<sup>3</sup>A enhances cross-band interaction via hierarchical spectral grouping and adjacent spectra shuffle. (b) TSA models complementary dependencies along spectral/height/width views and fuses them to recalibrate features. (c) MCR projects features to a compact spectral manifold and iteratively aggregates corrections for physically plausible spectra.

### 3 Method

#### 3.1 Overview

The entire pipeline of  $SR^2$ -Net is shown in Fig. 2, which is an end-to-end super-resolution network. Specifically, an SR model recovers the high-resolution HSI that is contained with spectral artifacts from the low-resolution input. We establish a novel Hierarchical Spectral-Spatial Synergy Attention (H-S<sup>3</sup>A) module, which enhances cross-band interactions using pyramidal grouping, trilateral synergy attention (TSA), and locality-preserving spectral shuffle. Then, a Manifold Consistency Rectification (MCR) module further refines the features by aligning them to a compact, physically plausible spectral manifold. After that, an optimization objective jointly trains the network with a reconstruction loss and an auxiliary degradation-consistency loss to ensure that the reconstructed HR image matches the LR observation after degradation.

#### 3.2 Super-Resolution Model

Given a low-resolution input  $I_{LR} \in \mathbb{R}^{h \times w \times S}$  with  $S$  ordered spectral bands, the SR backbone first produces an initial super-resolved reconstruction  $\tilde{I}_{SR} \in \mathbb{R}^{H \times W \times S}$  with an upscaling factor  $\alpha$ , where  $H = \alpha h$  and  $W = \alpha w$ .

Specifically, it first produces an initial SR prediction  $\tilde{I}_{SR}$  as:

$$\tilde{I}_{SR} = f_{SR}(I_{LR}), \quad (1)$$

where,  $f_{SR}(\cdot)$  denotes an SR model. Then, we feed  $\tilde{I}_{SR}$  into our proposed rectifier to suppress spectral oscillations and refine the results. This process is primarily achieved by two key

modules: H-S<sup>3</sup>A for cross-band interaction enhancement and MCR for manifold-consistency rectification.

#### 3.3 H-S<sup>3</sup>A: Cross-Band Interaction Enhancement

To enhance cross-band interactions and spectral reconstruction while preserving spatial details, we propose the H-S<sup>3</sup>A module. As shown in Fig. 2(a), H-S<sup>3</sup>A consists of three components: spectral grouping, trilateral synergy attention, and adjacent spectral shuffle.

**Spectral grouping.** We evenly split the ordered spectra of  $\tilde{I}_{SR} \in \mathbb{R}^{H \times W \times S}$  into four contiguous groups along the band dimension:  $\{G_1, G_2, G_3, G_4\}$ , where  $G_i \in \mathbb{R}^{H \times W \times S/4}$ . Then, each group is processed by convolutions with different receptive fields to capture complementary spatial contexts, producing  $\{G'_1, G'_2, G'_3, G'_4\}$ , which are then fed into TSA for subsequent interaction modeling.

**Trilateral Synergy Attention.** We apply TSA to each group feature to jointly capture spectral and spatial dependencies. For a given group feature  $G'_i \in \mathbb{R}^{H \times W \times S/4}$ , TSA first summarizes  $G'_i$  from three complementary views by average pooling:

$$A_i^d = \sigma(AvgPool_{d_i}(G'_i)), d_i = \{h, w, s\}, \quad (2)$$

where  $\sigma(\cdot)$  represents a series of convolutions, GeLU operations, and a sigmoid function. And  $A_i^h \in \mathbb{R}^{H \times 1 \times S/4}$  captures global spectral statistics, while  $A_i^w \in \mathbb{R}^{1 \times W \times S/4}$  and  $A_i^s \in \mathbb{R}^{1 \times 1 \times S/4}$  preserve coordinate contexts. These form

Dataset	Scale	Metric	CNN-based						Transformer-based						Diffusion-based		
			RCAN			SSPSR			SwinIR			ESSAformer			DDS2M		
			Base	+Ours	Gain	Base	+Ours	Gain	Base	+Ours	Gain	Base	+Ours	Gain	Base	+Ours	Gain
ARAD-1K	x2	mPSNR↑	48.7390	50.2735	+1.5345	46.0882	48.5005	+2.4123	50.4662	51.6551	+1.1889	49.4500	49.9900	+0.5400	36.5792	37.2283	+0.6491
		mSAM↓	1.2071	0.7849	-0.4222	0.9906	0.6658	-0.3248	0.7727	0.4842	-0.2885	0.6090	0.5080	-0.1010	7.1986	4.7788	-2.4199
		mSSIM↑	0.9936	0.9964	+0.0028	0.9893	0.9920	+0.0027	0.9972	0.9975	+0.0003	0.9937	0.9942	+0.0005	0.9089	0.9277	+0.0188
		CC↑	0.9978	0.9990	+0.0012	0.9960	0.9981	+0.0021	0.9990	0.9993	+0.0003	0.9986	0.9987	+0.0001	0.9723	0.9799	+0.0076
	x4	mPSNR↑	38.3786	40.0972	+1.7186	38.8792	40.1004	+1.2212	39.5717	40.9720	+1.4003	39.9537	40.7200	+0.7663	30.8476	33.2613	+2.4137
		mSAM↓	1.9009	1.3010	-0.5999	1.6076	1.3128	-0.2948	1.3950	1.2819	-0.1131	1.3670	1.2300	-0.1370	7.0404	5.8757	-1.1647
		mSSIM↑	0.9470	0.9719	+0.0249	0.9463	0.9543	+0.0080	0.9709	0.9752	+0.0043	0.9592	0.9599	+0.0007	0.7984	0.8671	+0.0687
		CC↑	0.9812	0.9916	+0.0104	0.9858	0.9891	+0.0033	0.9902	0.9924	+0.0022	0.9903	0.9904	+0.0001	0.9421	0.9549	+0.0128
	x8	mPSNR↑	33.3062	34.3745	+1.0683	34.1149	34.9975	+0.8826	33.4185	34.8318	+1.4133	34.6531	35.0546	+0.4015	27.7449	29.5794	+1.8345
		mSAM↓	3.0518	2.1900	-0.8618	2.4223	2.0352	-0.3871	2.4682	2.1164	-0.3518	2.3531	2.0140	-0.3391	11.5589	9.2067	-2.3522
		mSSIM↑	0.8891	0.9029	+0.0138	0.8724	0.8850	+0.0126	0.8869	0.9103	+0.0234	0.8882	0.8889	+0.0007	0.6060	0.7993	+0.1933
		CC↑	0.9628	0.9693	+0.0065	0.9622	0.9681	+0.0059	0.9551	0.9720	+0.0169	0.9691	0.9698	+0.0007	0.8861	0.9019	+0.0158
CAVE	x2	mPSNR↑	41.0944	43.4074	+2.3130	39.4003	40.4833	+1.0830	40.3123	41.4861	+1.1738	39.4700	40.7900	+1.3200	35.5928	36.5567	+0.9639
		mSAM↓	5.7619	4.4010	-1.3609	4.2518	3.7893	-0.4625	0.8214	0.6275	-0.1939	4.0820	3.3450	-0.7370	11.0914	8.1802	-2.9112
		mSSIM↑	0.9838	0.9897	+0.0059	0.9711	0.9830	+0.0119	0.9754	0.9877	+0.0123	0.9704	0.9747	+0.0043	0.9053	0.9357	+0.0304
		CC↑	0.9946	0.9965	+0.0019	0.9907	0.9943	+0.0036	0.9807	0.9905	+0.0098	0.9950	0.9960	+0.0010	0.9882	0.9908	+0.0026
	x4	mPSNR↑	35.9929	37.4461	+1.4532	35.2386	35.8929	+0.6543	37.2675	38.1303	+0.8628	34.1100	35.3300	+1.2200	29.8048	31.4389	+1.6341
		mSAM↓	7.6445	5.4742	-2.1703	4.8735	4.4121	-0.4614	0.9015	0.7083	-0.1932	5.6070	4.5410	-1.0660	13.7359	10.0409	-3.6950
		mSSIM↑	0.9536	0.9643	+0.0107	0.9384	0.9427	+0.0043	0.9492	0.9577	+0.0085	0.9267	0.9367	+0.0100	0.7493	0.8875	+0.1382
		CC↑	0.9825	0.9856	+0.0031	0.9795	0.9807	+0.0012	0.9315	0.9478	+0.0163	0.9846	0.9875	+0.0029	0.9699	0.9766	+0.0067
	x8	mPSNR↑	32.0839	33.2764	+1.1925	31.5901	32.0282	+0.4381	32.8788	34.2636	+1.3848	30.0600	30.8700	+0.8100	27.1577	28.1137	+0.9560
		mSAM↓	10.1641	6.8252	-3.3389	7.6479	6.1349	-1.5130	1.5060	0.8553	-0.6507	7.8170	6.0120	-1.8050	16.6298	13.7381	-2.8917
		mSSIM↑	0.8923	0.9104	+0.0181	0.8781	0.8828	+0.0047	0.9125	0.9321	+0.0196	0.8530	0.8664	+0.0134	0.6298	0.7948	+0.1650
		CC↑	0.9616	0.9654	+0.0038	0.9577	0.9599	+0.0022	0.9185	0.9233	+0.0048	0.9637	0.9683	+0.0046	0.9186	0.9389	+0.0203

Table 1: Main results on ARAD-1K and CAVE at  $\times 2$ ,  $\times 4$ , and  $\times 8$ . Five backbones are evaluated with and without  $SR^2$ -Net. We report mPSNR, mSSIM, mSAM, and CC, with higher being better except for mSAM. Gain denotes the change over the baseline.

the Trilateral Synergy Attention set  $\{A^h, A^w, A^s\}$ , and then the attention maps are fused to recalibrate the features as follows:

$$F_i = G'_i \odot (A_i^h \otimes A_i^w \otimes A_i^s), \quad (3)$$

where the operator  $\otimes$  denotes a linear combination of the three attention maps, and  $\odot$  denotes element-wise multiplication with broadcasting. Applying TSA to the four groups yields  $\{F_1, F_2, F_3, F_4\}$ .

**Adjacent Spectra Shuffle.** Although group-wise processing is efficient, it may restrict information exchange across groups. Inspired by the channel shuffle [Zhang *et al.*, 2018a], we introduce an adjacent spectra shuffle. Unlike a global shuffle, our design explicitly ensure the continuity of adjacent hyperspectral bands. Specifically, we concatenate the TSA-enhanced groups along the spectral dimension,  $F = [F_1, F_2, F_3, F_4] \in \mathbb{R}^{H \times W \times S}$ , where  $[\cdot]$  denotes concatenation. We then index the channels of each group as follows:

$$F_i \xrightarrow{\text{channel}} \{C_{n_i+1}, C_{n_i+2}, \dots, C_{n_i+\frac{S}{4}}\}, n_i = \frac{S}{4}(i-1). \quad (4)$$

To enable adjacent interaction, we swap the boundary channels between neighboring groups. For  $i = 2, 3, 4$ , the channel  $C_{n_i+1}$  is swapped with  $C_{n_i}$ , *i.e.*, the first channel of the  $i$ -th group is exchanged with the last channel of the  $(i-1)$ -th group. Similarly, for  $i = 1, 2, 3$ , the channel  $C_{n_i+\frac{S}{4}}$  is swapped with  $C_{n_i+\frac{S}{4}+1}$ , *i.e.*, the last channel of the  $i$ -th group

is exchanged with the first channel of the  $(i+1)$ -th group. Finally, we adjust the feature dimension of  $F_s \in \mathbb{R}^{H \times W \times S}$  and feed it into the MCR for further rectification.

### 3.4 MCR: Manifold-Consistency Rectification

Under the manifold assumption, natural data tend to lie on a low-dimensional manifold [Li and He, 2025; Chapelle *et al.*, 2006] and hyperspectral images follow the same principle. Based on this conclusion, we propose Manifold Consistency Rectification (MCR) to progressively rectify feature representations so that they remain aligned with the underlying spectral manifold.

As illustrated in Fig. 2(c), MCR first applies a Manifold Projection to map the input spectral feature  $F_s \in \mathbb{R}^{H \times W \times C}$  from the original channel dimension  $C$  to a reduced dimension  $r$ , producing an initial manifold embedding as follows:

$$m_0 = P(F_s) \in \mathbb{R}^{H \times W \times r}. \quad (5)$$

This compact embedding suppresses spectral redundancy and provides a suitable space for consistency rectification. Then MCR performs  $N$  stages of refinement. At the  $i$ -th stage, a Refine Block updates the manifold embedding by:

$$m_i = f_m(m_{i-1}), \quad i = 1, 2, \dots, N, \quad (6)$$

where  $f_m(\cdot)$  denotes the Refine Block. For each refined embedding  $m_i$ , a Back-Block generates a rectification component in the original channel space through  $g_m(m_i)$ . The final rectified output is obtained by aggregating the rectification

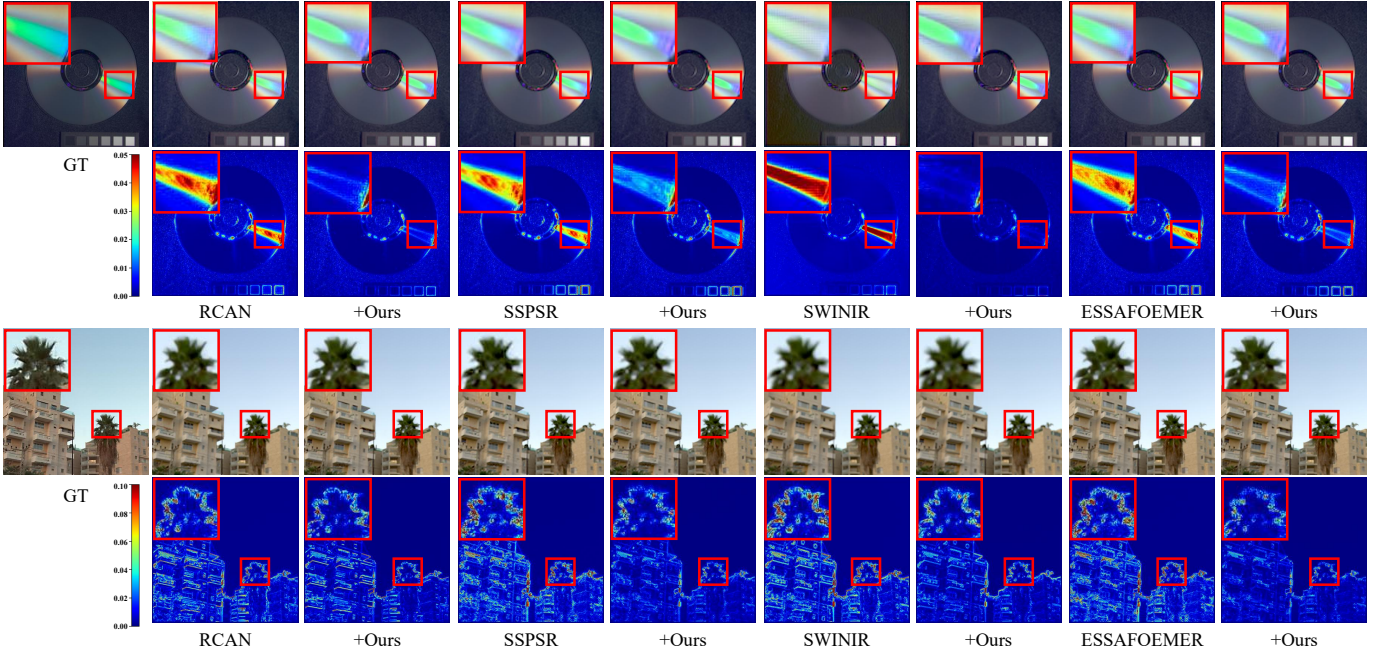


Figure 3: Qualitative comparisons on CAVE (top) and ARAD-1K (bottom) at the  $\times 4$  scale. Pseudo-RGB visualizations are rendered using spectral bands 25–15–5 as R–G–B, and the corresponding error maps are shown below each reconstruction. Red boxes highlight representative regions where  $SR^2$ -Net reduces reconstruction errors around edges and fine structures compared with the baselines.

components across all stages as:

$$\hat{I}_{SR} = \sum_{i=0}^N g_m(m_i). \quad (7)$$

This progressive rectification scheme encourages the learned representations to preserve spectral continuity while reducing manifold distortion introduced by preceding operations.

### 3.5 Degradation-Consistency Loss

The motivation behind the degradation-consistency loss is to enforce data fidelity for HSI-SR. We propose a simple yet effective strategy based on the principle that the predicted super-resolved HSI, after being subjected to the same degradation process, should be able to reproduce the observed low-resolution input.

Specifically, the predicted HR image  $\hat{I}_{SR}$  is first degraded to the LR space using bicubic downsampling. The resulting image is then compared with the input  $I_{LR}$ , leading to the degradation-consistency loss as follows:

$$\mathcal{L}_{deg} = \left\| \mathcal{D}(\hat{I}_{SR}) - I_{LR} \right\|_2^2, \quad (8)$$

where  $\mathcal{D}(\cdot)$  denotes the degradation model used to generate the LR input. Following the original setting of the SR model, we retain its standard  $\ell_2$  reconstruction loss, which is used to supervise the SR prediction, and the total loss is:

$$\mathcal{L}_{total} = \lambda_{rec} \cdot \mathcal{L}_{recon} + \lambda_{deg} \cdot \mathcal{L}_{deg}, \quad (9)$$

where  $\lambda_{rec}$  and  $\lambda_{deg}$  are balance terms. This loss encourages the super-resolved output to remain consistent with the physical degradation process, thereby improving spectral fidelity and suppressing hallucinated details.

## 4 Experiments

### 4.1 Experimental Settings

**Datasets.** We evaluate on three widely used hyperspectral datasets, ARAD-1K [Arad *et al.*, 2022], CAVE [Park *et al.*, 2007], and ICVL [Arad and Ben-Shahar, 2016], each providing 31-band HSIs. ARAD-1K contains 950 images, where we follow the standard split of 900 for training and 50 for testing. CAVE includes 32 scenes, with 16 used for training and the remaining 16 for testing. ICVL contains 18 HSIs which is used only for cross-domain evaluation.

**Degradation model.** Low-resolution inputs are synthesized from HR images using bicubic downsampling with scale factors. To assess robustness to degradation mismatch, we keep this training setup unchanged and replace the test-time degradation with alternative settings in the appendix 2.4, including different downsampling kernels as well as additional blur and noise.

**Evaluation metrics.** We evaluate spatial reconstruction using the mean peak signal-tonoise ratio (mPSNR)[Chan and Whiteman, 2007] and mean structure similarity (mSSIM) [Wang, 2004], and spectral fidelity using mean spectral angle mapper (mSAM)[Kruse *et al.*, 1993] and the mean spectral correlation coefficient (CC)[Loncan *et al.*, 2015]. mPSNR and mSSIM are averaged over all 31 bands, while mSAM and CC are averaged over pixels and images. For brevity, appendix tables report mPSNR, mSSIM, and mSAM.

**Compared methods.** To verify plug-and-play generality, we attach  $SR^2$ -Net to five representative baseline models: CNN-based RCAN [Zhang *et al.*, 2018b] and SSPSR [Jiang *et al.*, 2020], Transformer-based SwinIR [Liang *et al.*, 2021]

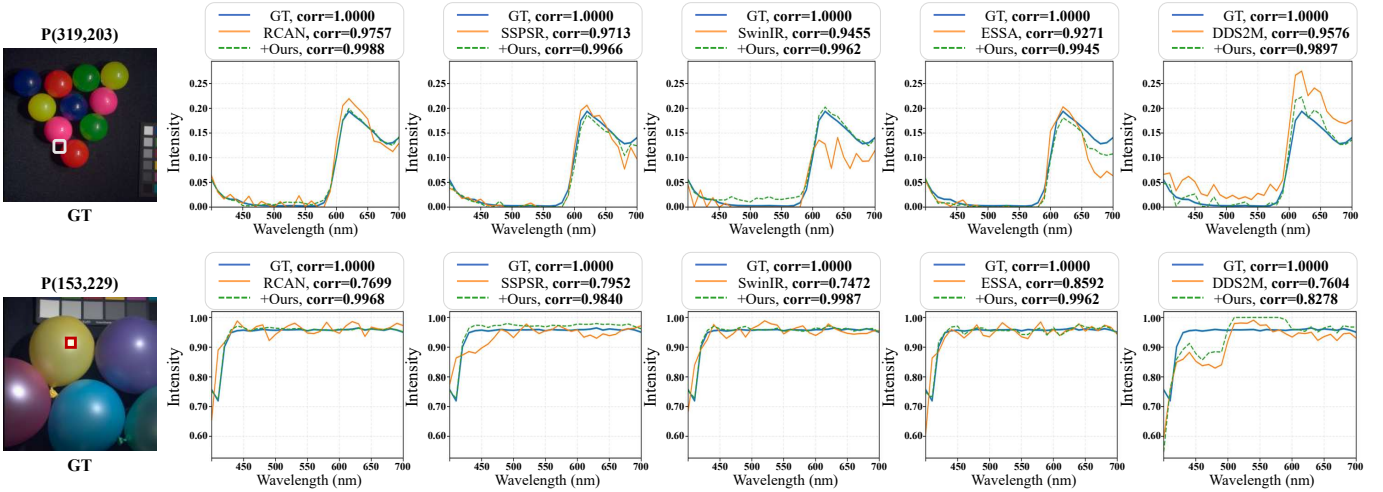


Figure 4: Spectral fidelity visualization on CAVE dataset at the  $\times 4$  scale. For two representative pixels (marked in the left pseudo-RGB images), we plot the ground-truth spectra (GT), the baseline backbone outputs, and the corresponding results after attaching  $SR^2$ -Net. While GT spectra may contain mild fluctuations, baseline reconstructions often exhibit abnormal cross-band deviations or spurious oscillations;  $SR^2$ -Net suppresses these non-physical behaviors and produces spectra that better follow the GT trend across different backbones.

Method	Scale	Variant	CAVE			ICVL		
			mPSNR↑	mSSIM↑	mSAM↓	mPSNR↑	mSSIM↑	mSAM↓
RCAN	$\times 2$	Base	42.7269	0.9866	5.0004	49.6448	0.9976	0.7389
		+Ours	44.2866	0.9886	4.0978	51.8506	0.9979	0.4682
		Gain	+1.5597	+0.0020	-0.9026	+2.2058	+0.0003	-0.2707
	$\times 4$	Base	35.6214	0.9537	6.2153	39.9389	0.9707	1.0969
		+Ours	36.3326	0.9576	5.3594	40.9148	0.9723	0.7897
		Gain	+0.7112	+0.0039	-0.8559	+0.9759	+0.0016	-0.3072
SSPSR	$\times 2$	Base	41.4071	0.9816	4.0419	48.4758	0.9966	0.8140
		+Ours	43.0076	0.9845	2.9243	50.7217	0.9972	0.5264
		Gain	+1.6005	+0.0029	-1.1176	+2.2459	+0.0006	-0.2876
	$\times 4$	Base	36.7963	0.9521	4.9284	43.9812	0.9851	1.0271
		+Ours	37.5721	0.9557	3.9189	45.1945	0.9856	0.6698
		Gain	+0.7758	+0.0036	-1.0095	+1.2133	+0.0005	-0.3573
SwinIR	$\times 2$	Base	40.7157	0.9839	4.4366	47.9367	0.9964	0.8260
		+Ours	42.3415	0.9877	2.6231	50.0704	0.9971	0.4709
		Gain	+1.6258	+0.0038	-1.8135	+2.1337	+0.0007	-0.3551
	$\times 4$	Base	34.7725	0.9313	4.8551	41.0743	0.9708	1.0552
		+Ours	35.7256	0.9577	3.8360	42.6530	0.9799	0.6682
		Gain	+0.9531	+0.0264	-1.0191	+1.5787	+0.0091	-0.3870
ESSAformer	$\times 2$	Base	42.1763	0.9835	3.3575	49.7895	0.9973	0.6404
		+Ours	43.4978	0.9855	2.5611	51.3981	0.9977	0.4625
		Gain	+1.3215	+0.0020	-0.7964	+1.6086	+0.0004	-0.1779
	$\times 4$	Base	37.0305	0.9556	4.8258	44.3869	0.9856	0.9349
		+Ours	37.6350	0.9579	3.5556	45.7012	0.9866	0.6079
		Gain	+0.6045	+0.0023	-1.2702	+1.3143	+0.0010	-0.3270

Table 2: Cross-domain results (trained on ARAD-1K, tested on CAVE and ICVL without fine-tuning). Base denotes each backbone trained on ARAD-1K and directly evaluated on CAVE and ICVL. +Ours denotes the same backbone augmented with  $SR^2$ -Net, trained on ARAD-1K, and directly evaluated on CAVE and ICVL.

and ESSAformer [Zhang *et al.*, 2023], and diffusion-based DDS2M [Miao *et al.*, 2023].

For each SR backbone  $\mathcal{B}$ , we retrain the baseline  $\mathcal{B}$  and the end-to-end rectified version  $\mathcal{B} + SR^2$ -Net under the same settings, and report their results side by side.

**Implementation details.** All methods are implemented in PyTorch and retrained end-to-end on an NVIDIA RTX 3090 GPU. We use AdamW with  $\beta_1 = 0.9$  and  $\beta_2 = 0.99$ . The learning rate starts from  $1 \times 10^{-4}$  and is decayed to  $1 \times 10^{-5}$  via cosine annealing. Models are trained for 1000 epochs with batch size 8 using cropped LR patches. The LR patch sizes for  $\times 2$ ,  $\times 4$ , and  $\times 8$  are  $64 \times 64$ ,  $32 \times 32$ , and  $32 \times 32$ , with corresponding HR sizes of  $128 \times 128$ ,  $128 \times 128$ , and  $256 \times 256$ . We optimize the  $\ell_2$  reconstruction loss together with the degradation-consistency loss, with  $\lambda_{\text{rec}} = 1.0$  and  $\lambda_{\text{deg}} = 0.2$ . Tab. 5 varies  $\lambda_{\text{deg}}$  while keeping other settings fixed.  $SR^2$ -Net uses 4 spectral groups, 4 H-S<sup>3</sup>A blocks, and 1 MCR block with bottleneck rank  $r = 8$ .

## 4.2 Quantitative Results and Analysis

We evaluate  $SR^2$ -Net under two evaluation strategies. One strategy measures in-domain performance by training and testing within ARAD-1K and within CAVE using the standard splits, and reports results at  $\times 2$ ,  $\times 4$ , and  $\times 8$  in Tab. 1. The other strategy measures cross-domain generalization by training on the 900 training images of ARAD-1K and directly testing on all CAVE scenes and all ICVL HSIs without fine-tuning, and reports results at  $\times 2$  and  $\times 4$  in Tab. 2.

**In-domain performance.** Tab. 1 shows that attaching  $SR^2$ -Net consistently improves spectral fidelity across backbones and scales, reflected by lower mSAM in every setting. Spatial quality is preserved and often improved, suggesting that the rectifier suppresses non-physical spectral artifacts without sacrificing fine details. For example, on CAVE at  $\times 4$ , RCAN improves mPSNR from 35.9929 to 37.4461 while reducing mSAM from 7.6445 to 5.4742. We further observe that the benefit becomes more pronounced for backbones that tend to produce stronger spectral artifacts, including diffusion-based reconstructions.

Scale	Method	Params (M)	FLOPs (G)
$\times 4$	Baseline	8.228	19.302
	+Ours	8.276	20.785
$\times 8$	Baseline	8.376	25.891
	+Ours	8.424	27.373

Table 3: Model complexity of SwinIR with  $SR^2$ -Net under different scales.

Method		Metric			$\lambda_{\text{rec}}$	$\lambda_{\text{deg}}$	mPSNR $\uparrow$	mSSIM $\uparrow$	mSAM $\downarrow$
<b>H-S<sup>3</sup>A</b>	MCR	mPSNR $\uparrow$	mSSIM $\uparrow$	mSAM $\downarrow$	1.0	0.0	40.6920	0.9740	1.3262
$\times$	$\times$	39.5717	0.9709	1.3950	1.0	0.1	<b>40.9720</b>	<b>0.9752</b>	<b>1.2819</b>
$\checkmark$	$\times$	40.7059	0.9735	1.3476	1.0	0.2	40.9225	0.9751	1.2833
$\times$	$\checkmark$	40.2550	0.9717	1.3173	1.0	0.5	40.7184	0.9745	1.3174
$\checkmark$	$\checkmark$	<b>40.9720</b>	<b>0.9752</b>	<b>1.2819</b>	1.0	1.0	40.6217	0.9739	1.3305

Table 4: Component ablation on ARAD-1K at the  $\times 4$  scale using SwinIR as the SR model.

Table 5: Loss weight ablation on ARAD-1K at the  $\times 4$  scale using SwinIR with  $SR^2$ -Net.

**Cross-domain generalization.** Tab. 2 confirms that the improvements persist under domain shift. Models trained on ARAD-1K generalize better after attaching  $SR^2$ -Net, with consistent mSAM reductions on both CAVE and ICVL while maintaining or improving spatial metrics. For instance, SwinIR on CAVE at  $\times 2$  improves mPSNR from 40.7157 to 42.3415 and reduces mSAM from 4.4366 to 2.6231.

**Efficiency and overhead.**  $SR^2$ -Net is lightweight and introduces minor overhead. As summarized in Tab. 3, SwinIR at  $\times 4$  increases from 8.228 to 8.276 parameters and from 19.302 to 20.785 FLOPs, with a similar trend at higher scales. Additional runtime and robustness results, including comparisons to simple post-hoc spectral rectifiers, are provided in the appendix 2.3.

### 4.3 Visualization

**Qualitative comparisons.** Fig. 3 shows the pseudo-RGB reconstructions together with error maps at the  $\times 4$  scale. Pseudo-RGB images are rendered by mapping bands 25, 15, and 5 to the R/G/B channels. The top row shows examples from CAVE and the bottom row shows examples from ARAD-1K. Across backbones, a typical failure case of baseline SR models is the appearance of spatially localized artifacts near object boundaries and thin structures. Such regions are especially sensitive to cross-band inconsistencies and often manifest as boundary halos or edge misalignment across bands. After attaching  $SR^2$ -Net, these boundary-related errors are visibly reduced in the highlighted areas while fine textures and sharp edges are preserved, indicating that the rectifier mainly corrects band-inconsistent distortions rather than smoothing the reconstruction. For additional error maps of ARAD-1K, CAVE, and ICVL, please refer to the appendix 2.1.

**Spectral fidelity visualization.** Fig. 4 visualizes per-pixel spectra at two selected locations on CAVE under  $\times 4$  upsampling. While baseline SR models can recover plausible spatial details, their reconstructed spectra may exhibit non-physical

band-to-band oscillations, resulting in jagged curves that deviate from the ground-truth trend.  $SR^2$ -Net suppresses these oscillations and yields smoother, more coherent spectral profiles that better follow the ground truth across different backbones. This visual evidence aligns with the consistent reductions in mSAM reported in the quantitative results. Additional spectral-curve visualizations on ARAD-1K, CAVE, and ICVL are provided in the appendix 2.2.

### 4.4 Ablation Study

To analyze the contributions of different components in  $SR^2$ -Net, we conduct an ablation study, as shown in Tab 4. All ablations are conducted on ARAD-1K at the  $\times 4$  scale using SwinIR.

**Component ablation.** Tab. 4 evaluates the two-stage design of  $SR^2$ -Net. H-S<sup>3</sup>A mainly strengthens cross-band interactions and improves spatial reconstruction, while MCR focuses on spectral plausibility by suppressing band-inconsistent oscillations. When used together, the two components are complementary: H-S<sup>3</sup>A makes the representation more coherent across bands, and MCR further removes non-physical fluctuations while preserving informative details. As a representative example, the full model reaches 40.9720 mPSNR and 1.2819 mSAM on ARAD-1K at  $\times 4$ , achieving a balanced improvement in both spatial and spectral quality. For completeness, we also compare against low-cost spectral rectifiers (Savitzky-Golay, PCA projection, and Iterative Back-projection) in the appendix 2.5; these methods can partially smooth spectra or enforce measurement consistency, but they do not jointly model spectral structure and spatial detail restoration as an end-to-end rectifier.

**Degradation-consistency loss.** Tab. 5 studies the weight of degradation-consistency  $\lambda_{\text{deg}}$ . Without this term, spectral fidelity degrades, indicating that HR supervision alone may not sufficiently penalize band-inconsistent artifacts. A moderate  $\lambda_{\text{deg}}$  gives the best overall performance, while overly large values slightly hurt results, suggesting an overly strict constraint can hinder detail preservation. Overall, the degradation-consistency term complements the proposed rectification by discouraging reconstructions that are inconsistent with the assumed observation process.

## 5 Conclusion

In this paper, We presented  $SR^2$ -Net, a lightweight plug-and-play rectifier for hyperspectral image super-resolution. By decoupling spectral correction from SR backbones,  $SR^2$ -Net can be attached to diverse CNN-, Transformer-, and diffusion-based models with negligible overhead. Experiments across multiple benchmarks and scales show consistent gains in spectral fidelity while preserving (often improving) spatial quality, suggesting that  $SR^2$ -Net mainly corrects band-inconsistent distortions rather than over-smoothing details. Ablations confirm the complementarity of cross-band interaction enhancement and manifold-guided rectification, and highlight the benefit of degradation consistency for data fidelity. Future work will extend  $SR^2$ -Net to more realistic degradations and evaluate its impact on downstream hyperspectral applications.

## References

[Aburaed *et al.*, 2023] Nour Aburaed, Mohammed Q Alkhatib, Stephen Marshall, Jaime Zabalza, and Hussain Al Ahmad. A review of spatial enhancement of hyperspectral remote sensing imaging techniques. *IEEE Journal of Selected Topics in Applied Earth Observations and Remote Sensing*, 16:2275–2300, 2023.

[Arad and Ben-Shahar, 2016] Boaz Arad and Ohad Ben-Shahar. Sparse recovery of hyperspectral signal from natural rgb images. In *European conference on computer vision*, pages 19–34. Springer, 2016.

[Arad *et al.*, 2022] Boaz Arad, Radu Timofte, Rony Yahel, Nimrod Morag, Amir Bernat, Yuanhao Cai, Jing Lin, Zudi Lin, Haoqian Wang, Yulun Zhang, Hanspeter Pfister, Luc Van Gool, Shuai Liu, Yongqiang Li, Chaoyu Feng, Lei Lei, Jiaojiao Li, Songcheng Du, Chaoxiong Wu, Yihong Leng, Rui Song, Mingwei Zhang, Chongxing Song, Shuyi Zhao, Zhiqiang Lang, Wei Wei, Lei Zhang, Renwei Dian, Tiansi Shan, Anjing Guo, Chengguo Feng, Jinyang Liu, Mirko Agarla, Simone Bianco, Marco Buzzelli, Luigi Celona, Raimondo Schettini, Jiang He, Yi Xiao, Jiajun Xiao, Qiangqiang Yuan, Jie Li, Liangpei Zhang, Tae-sung Kwon, Dohoon Ryu, Hyokyoung Bae, Hao-Hsiang Yang, Hua-En Chang, Zhi-Kai Huang, Wei-Ting Chen, Sy-Yen Kuo, Junyu Chen, Haiwei Li, Song Liu, Sabarinathan, K Uma, B Sathya Bama, and S. Mohamed Mansoor Roomi. Ntire 2022 spectral recovery challenge and data set. In *Proceedings of the IEEE/CVF Conference on Computer Vision and Pattern Recognition (CVPR) Workshops*, pages 863–881, June 2022.

[Chan and Whiteman, 2007] Luen C Chan and Peter Whiteman. Hardware-constrained hybrid coding of video imagery. *IEEE Transactions on Aerospace and Electronic Systems*, (1):71–84, 2007.

[Chapelle *et al.*, 2006] Olivier Chapelle, Bernhard Schölkopf, and Alexander Zien. *Semi-Supervised Learning*. The MIT Press, 09 2006.

[Chen *et al.*, 2023] Xiangyu Chen, Xintao Wang, Jiantao Zhou, and Chao Dong. Activating more pixels in image super-resolution transformer. In *Proceedings of the IEEE/CVF Conference on Computer Vision and Pattern Recognition (CVPR)*, pages 22367–22377, 2023.

[Fu *et al.*, 2016] Ying Fu, Yinqiang Zheng, Imari Sato, and Yoichi Sato. Exploiting spectral-spatial correlation for coded hyperspectral image restoration. In *Proceedings of the IEEE Conference on Computer Vision and Pattern Recognition*, pages 3727–3736, 2016.

[Gao *et al.*, 2025] Feng Gao, Xuepeng Jin, Xiaowei Zhou, Junyu Dong, and Qian Du. Msfmamba: Multi-scale feature fusion state space model for multi-source remote sensing image classification. *IEEE Transactions on Geoscience and Remote Sensing*, 2025.

[Guo *et al.*, 2024] Hang Guo, Jinmin Li, Tao Dai, Zhi Ouyang, Xidong Ren, and Shu-Tao Xia. Mambair: A simple baseline for image restoration with state-space model. In *European Conference on Computer Vision (ECCV)*, 2024.

[He *et al.*, 2024] Chengxun He, Yang Xu, Zebin Wu, and Zhihui Wei. Connecting low-level and high-level visions: A joint optimization for hyperspectral image super-resolution and target detection. *IEEE Transactions on Geoscience and Remote Sensing*, 62:1–16, 2024.

[Jiang *et al.*, 2020] Junjun Jiang, He Sun, Xianming Liu, and Jiayi Ma. Learning spatial-spectral prior for super-resolution of hyperspectral imagery. *IEEE Transactions on Computational Imaging*, 6:1082–1096, 2020.

[Kotwal *et al.*, 2025] Alankar Kotwal, Vishwanath Saragadam, Joshua D Bernstock, Alfredo Sandoval, Ashok Veeraraghavan, and Pablo A Valdés. Hyperspectral imaging in neurosurgery: a review of systems, computational methods, and clinical applications. *Journal of biomedical optics*, 30(2):023512–023512, 2025.

[Kruse *et al.*, 1993] Fred A Kruse, Adam B Lefkoff, Joseph W Boardman, Kathleen B Heidebrecht, AT Shapiro, PJ Barloon, and Alexander FH Goetz. The spectral image processing system (sips)—interactive visualization and analysis of imaging spectrometer data. *Remote sensing of environment*, 44(2-3):145–163, 1993.

[Li and He, 2025] Tianhong Li and Kaiming He. Back to basics: Let denoising generative models denoise. *arXiv preprint arXiv:2511.13720*, 2025.

[Liang *et al.*, 2021] Jingyun Liang, Jie Zhang, Guolei Sun, Kai Zhang, Luc Van Gool, and Radu Timofte. Swinir: Image restoration using swin transformer. In *Proceedings of the IEEE/CVF international conference on computer vision*, pages 1833–1844, 2021.

[Lin *et al.*, 2023] Xinqi Lin, Jingwen He, Zongsheng Chen, Zhibo Zhou, and Chao Dong. Diffbir: Towards blind image restoration with generative diffusion prior. In *Proceedings of the IEEE/CVF International Conference on Computer Vision (ICCV)*, pages 4339–4349, 2023.

[Liu *et al.*, 2024] Yue Liu, Yunjie Tian, Yuzhong Zhao, Hongtian Yu, Lingxi Xie, Yaowei Wang, Qixiang Ye, and Yunfan Liu. Vmamba: Visual state space model. In *Proceedings of the IEEE/CVF Conference on Computer Vision and Pattern Recognition (CVPR)*, pages 1589–1600, 2024.

[Loncan *et al.*, 2015] Laetitia Loncan, Luis B De Almeida, José M Bioucas-Dias, Xavier Briottet, Jocelyn Chanussot, Nicolas Dobigeon, Sophie Fabre, Wenzhi Liao, Giorgio A Licciardi, Miguel Simoes, et al. Hyperspectral pansharpening: A review. *IEEE Geoscience and remote sensing magazine*, 3(3):27–46, 2015.

[Miao *et al.*, 2023] Yuchun Miao, Lefei Zhang, Liangpei Zhang, and Dacheng Tao. Dds2m: Self-supervised denoising diffusion spatio-spectral model for hyperspectral image restoration. In *Proceedings of the IEEE/CVF International Conference on Computer Vision*, pages 12086–12096, 2023.

[Pang *et al.*, 2024] Li Pang, Xiangyu Rui, Long Cui, Hongzhong Wang, Deyu Meng, and Xiangyong Cao. Hir-

diff: Unsupervised hyperspectral image restoration via improved diffusion models. In *Proceedings of the IEEE/CVF Conference on Computer Vision and Pattern Recognition*, pages 3005–3014, 2024.

[Park *et al.*, 2007] Jong-Il Park, Moon-Hyun Lee, Michael D Grossberg, and Shree K Nayar. Multispectral imaging using multiplexed illumination. In *2007 IEEE 11th International Conference on Computer Vision*, pages 1–8. IEEE, 2007.

[Wang *et al.*, 2021] Chunying Wang, Baohua Liu, Lipeng Liu, Yanjun Zhu, Jialin Hou, Ping Liu, and Xiang Li. A review of deep learning used in the hyperspectral image analysis for agriculture. *Artificial Intelligence Review*, 54(7):5205–5253, 2021.

[Wang *et al.*, 2024] Nan Wang, Shaohui Mei, Yifan Zhang, Mingyang Ma, and Xiangqing Zhang. Hyperspectral image reconstruction from rgb input through highlighting intrinsic properties. *IEEE Transactions on Geoscience and Remote Sensing*, 2024.

[Wang, 2004] Z Wang. Image quality assessment: Form error visibility to structural similarity. *IEEE Trans. Image Process.*, 13(4):604–606, 2004.

[Wu *et al.*, 2024] Suqin Wu, Kefei Zhang, Xuexi Liu, Shuangshuang Shi, Chaofa Bian, et al. Unsupervised blind spectral–spatial cross-super-resolution network for hsi and msi fusion. *IEEE Transactions on Geoscience and Remote Sensing*, 62:1–14, 2024.

[Yang *et al.*, 2025] Chen Yang, Zhiming Guo, Douglas Fernandes Barbin, Zhiqiang Dai, Nicholas Watson, Megan Povey, and Xiaobo Zou. Hyperspectral imaging and deep learning for quality and safety inspection of fruits and vegetables: A review. *Journal of Agricultural and Food Chemistry*, 73(17):10019–10035, 2025.

[Yue *et al.*, 2023] Zongsheng Yue, Jianyi Wang, and Chen Change Loy. Resshift: Efficient diffusion model for image super-resolution by residual shifting. In *Advances in Neural Information Processing Systems (NeurIPS)*, volume 36, pages 13294–13306, 2023.

[Zhang *et al.*, 2018a] Xiangyu Zhang, Xinyu Zhou, Mengxiao Lin, and Jian Sun. Shufflenet: An extremely efficient convolutional neural network for mobile devices. In *Proceedings of the IEEE conference on computer vision and pattern recognition*, pages 6848–6856, 2018.

[Zhang *et al.*, 2018b] Yulun Zhang, Kunpeng Li, Kai Li, Lichen Wang, Bineng Zhong, and Yun Fu. Image super-resolution using very deep residual channel attention networks. In *Proceedings of the European conference on computer vision (ECCV)*, pages 286–301, 2018.

[Zhang *et al.*, 2023] Mingjin Zhang, Chi Zhang, Qiming Zhang, Jie Guo, Xinbo Gao, and Jing Zhang. Es-saformer: Efficient transformer for hyperspectral image super-resolution. In *Proceedings of the IEEE/CVF International Conference on Computer Vision*, pages 23073–23084, 2023.

[Zhang *et al.*, 2025] Zhanxu Zhang, Linzi Yang, Guanlian Zhang, Jiangwei Deng, Lifeng Bian, and Chen Yang. Cassnet: Cross-attention enhanced spectral-spatial interaction network for hyperspectral image super-resolution. *IEEE Journal of Selected Topics in Applied Earth Observations and Remote Sensing*, 2025.

[Zheng *et al.*, 2021] Xiangtao Zheng, Wenjing Chen, and Xiaoqiang Lu. Spectral super-resolution of multispectral images using spatial–spectral residual attention network. *IEEE Transactions on Geoscience and Remote Sensing*, 60:1–14, 2021.

# SR<sup>2</sup>-Net: A General Plug-and-Play Model for Spectral Refinement in Hyperspectral Image Super-Resolution

## Supplementary Material

## 1 Method

### 1.1 H-S<sup>3</sup>A: Cross-Band Interaction Enhancement

**Convolutions after spectral grouping.** After spectral grouping, we apply a lightweight convolutional stem *within each group* before entering TSA. Specifically, each group is processed by a set of convolutions with complementary receptive fields, including a identity, a standard  $3 \times 3$  convolution, a  $5 \times 5$  depthwise convolution, and a  $3 \times 3$  dilated convolution, followed by a  $1 \times 1$  convolution for channel mixing and projection.

**Handling non-divisible channel grouping in H-S<sup>3</sup>A.** H-S<sup>3</sup>A performs group-wise spectral processing, which requires the spectral channel number to be divisible by the group size. When this condition is not met, we pad the input along the channel dimension with additional channels so that the padded channel number becomes divisible by the number of groups.

### 1.2 Manifold-Consistency Rectification Details

The MCR module consists of three key components, namely the *Manifold Block*, *Refine Block*, and *Back-Block*.

The *Manifold Block* is designed to project high-dimensional spectral features onto a low-dimensional manifold. It is composed of a  $1 \times 1$  convolution followed by a GeLU activation function, where the  $1 \times 1$  convolution reduces the channel dimension from  $C$  to  $r$ .

The *Refine Block* operates in the manifold space to progressively refine the embedded features. It shares a similar structure with the Manifold Block, consisting of a  $1 \times 1$  convolution and a GeLU activation function, while keeping the channel dimension unchanged at  $r$ .

The *Back-Block* maps the refined manifold features back to the original spectral space and generates the corresponding rectification components. It comprises a  $3 \times 3$  convolution, a GeLU activation function, and a  $1 \times 1$  convolution, and adopts a residual formulation. The computation can be expressed as

$$f_{\text{output}} = \text{Conv}_{1 \times 1}(\text{GeLU}(\text{Conv}_{3 \times 3}(f_{\text{input}})) + f_{\text{input}}), \quad (1)$$

where the final  $1 \times 1$  convolution expands the channel dimension from  $r$  back to  $C$ .

## 2 Experiments

### 2.1 Full Error Map Gallery

We provide representative error-map visualizations on ARAD-1K, CAVE, and ICVL to complement the quantitative results, as shown in Figs. 1–3. Each page contains two test scenes. For each scene, we show the pseudo-RGB rendering and the corresponding error maps of different SR backbones, where the rectified variant is placed next to its baseline for direct comparison.

Given a reconstructed HSI  $\hat{\mathbf{I}}_{\text{HR}}$  and the ground truth  $\mathbf{I}_{\text{HR}}$  with  $S = 31$  spectral bands, we compute a per-pixel error map by averaging the absolute reconstruction error across bands:

$$E(i, j) = \frac{1}{S} \sum_{s=1}^S \left| \hat{\mathbf{I}}_{\text{HR}}(i, j, s) - \mathbf{I}_{\text{HR}}(i, j, s) \right|. \quad (2)$$

For consistent display, we apply per-image min–max normalization and obtain  $\tilde{E} \in [0, 1]$ :

$$\tilde{E} = \frac{E - \min(E)}{\max(E) - \min(E)}, \quad (3)$$

where  $\min(\cdot)$  and  $\max(\cdot)$  are computed over all pixels within the same image. Pseudo-RGB images are rendered by mapping bands 25, 15, and 5 to the red, green and blue channels, followed by the same linear min–max stretch and clipping to  $[0, 1]$  for all methods.

As illustrated in Figs. 1–3, darker regions indicate smaller reconstruction error, while brighter regions highlight locations where the reconstruction deviates from the ground truth. Across datasets, the dominant errors of baseline models typically concentrate on object boundaries, thin structures, and high-frequency textures, where cross-band inconsistency is more likely to appear as visible artifacts. By placing the rectified outputs next to the corresponding baselines, the gallery highlights that  $SR^2$ -Net mainly suppresses boundary-related errors without washing out fine details.

## 2.2 Additional Spectral Curve Visualizations

We provide additional per-pixel spectral curve visualizations on ARAD-1K, CAVE, and ICVL to complement the quantitative comparisons and the spectral example in the main paper, as shown in Figs. 4–6. Each page contains two test scenes. For each scene, we mark two pixels on the pseudo-RGB rendering and plot the spectral signatures over all 31 bands for the ground truth, the baseline output, and the rectified output obtained by appending  $SR^2$ -Net.

All results are reported at the  $\times 4$  scale. Pseudo-RGB images are rendered by mapping bands 25, 15, and 5 to the RGB channels. The plots include CNN-, Transformer-, and Diffusion-based backbones, and DDS2M is visualized together with the other models under the same setting.

Real hyperspectral signatures typically vary smoothly with wavelength. In contrast, baseline SR models may introduce band-to-band oscillations, local spectral shifts, or distorted peak/valley structures at certain pixels. The rectified outputs consistently better follow the ground-truth trend and suppress non-physical oscillations while preserving the overall spectral shape, including the more challenging diffusion-based reconstructions. These observations align with the consistent improvements in spectral fidelity reported in the main paper.

## 2.3 Model Complexity Across Backbones and Scales

**Protocol.** We report the number of parameters and FLOPs for each SR backbone and its rectified variant (+  $SR^2$ -Net). FLOPs are measured on LR inputs of size  $64 \times 64$  for  $\times 2$  and  $32 \times 32$  for  $\times 4, \times 8$ , following the patch sizes used in training.

Scale	Metric	ESSAformer			RCAN			SSPSR			SwinIR		
		Base	+Ours	Gain	Base	+Ours	Gain	Base	+Ours	Gain	Base	+Ours	Gain
$\times 2$	Params (M)	8.686	8.734	+0.048	15.479	15.527	+0.048	10.534	10.581	+0.048	8.080	8.128	+0.048
	FLOPs (G)	431.388	432.871	+1.482	126.149	127.632	+1.482	219.438	220.920	+1.482	70.621	72.104	+1.482
$\times 4$	Params (M)	11.194	11.242	+0.048	15.627	15.675	+0.048	12.894	12.942	+0.048	8.228	8.276	+0.048
	FLOPs (G)	409.202	410.684	+1.482	33.208	34.690	+1.482	122.200	123.682	+1.482	19.302	20.785	+1.482
$\times 8$	Params (M)	13.702	13.750	+0.048	15.774	15.822	+0.048	15.254	15.302	+0.048	8.376	8.423	+0.048
	FLOPs (G)	1614.620	1620.549	+5.930	39.889	45.819	+5.930	391.559	397.488	+5.930	25.891	31.821	+5.930

Table 1: Parameters and FLOPs across backbones and scales (ARAD-1K checkpoints). We report the model size (Params, in millions) and computational cost (FLOPs, in billions).  $\Delta$  denotes the additional cost introduced by  $SR^2$ -Net.

**Takeaway.**  $SR^2$ -Net consistently introduces a constant parameter overhead (+0.048M) across backbones. The FLOPs overhead mainly depends on the HR spatial size:  $\times 2 / \times 4$  share the same HR patch size ( $128^2$ ), leading to +1.482G FLOPs, while  $\times 8$  uses  $256^2$ , resulting in +5.930G FLOPs.

## 2.4 Robustness to Test-Time Degradation Mismatch

**Degradation settings.** All models are trained with the standard synthetic degradation used in the main paper, where the low-resolution input is obtained by bicubic downsampling from the high-resolution hyperspectral image. We then test robustness under mild mismatch by keeping the trained model fixed and changing the test-time degradation in four ways. First, we vary the downsampling operator by replacing the training bicubic implementation with either area-based downsampling or an alternative bicubic implementation. Second, we introduce Gaussian blur in the high-resolution space before downsampling with blur standard deviation  $\sigma \in \{0.6, 1.0\}$ . The blur is applied independently to each spectral band using depthwise convolution with reflect padding, and the kernel size follows  $k = \max(3, 2\lceil 6\sigma \rceil + 1)$ , which results in  $k = 5$  for  $\sigma = 0.6$  and  $k = 7$  for  $\sigma = 1.0$ . Third, we add i.i.d. Gaussian noise in the low-resolution space after downsampling with  $\epsilon \sim \mathcal{N}(0, \sigma^2)$  and  $\sigma = n/255$ , where  $n \in \{1, 2, 5\}$ . Finally, we evaluate two combined settings with blur and noise pairs  $(\sigma, n) \in \{(0.6, 2), (1.0, 5)\}$ . For each scale factor, we center-crop high-resolution images so that both spatial dimensions are divisible by the scale. Noise is generated with a deterministic per-image seed to ensure reproducibility. Tab. 2 reports the results on ARAD-1K for SwinIR and SwinIR +  $SR^2$ -Net.

**Observation.** Across all mismatch settings and scales,  $SR^2$ -Net consistently improves spectral fidelity, as evidenced by lower mSAM. The advantage becomes more noticeable when the test-time operator deviates from the training downsampling implementation and when blur or noise is present. At the same time, spatial quality is generally preserved or improved, suggesting that the rectifier mitigates spectral inconsistency without sacrificing spatial reconstruction under mild degradation shifts.

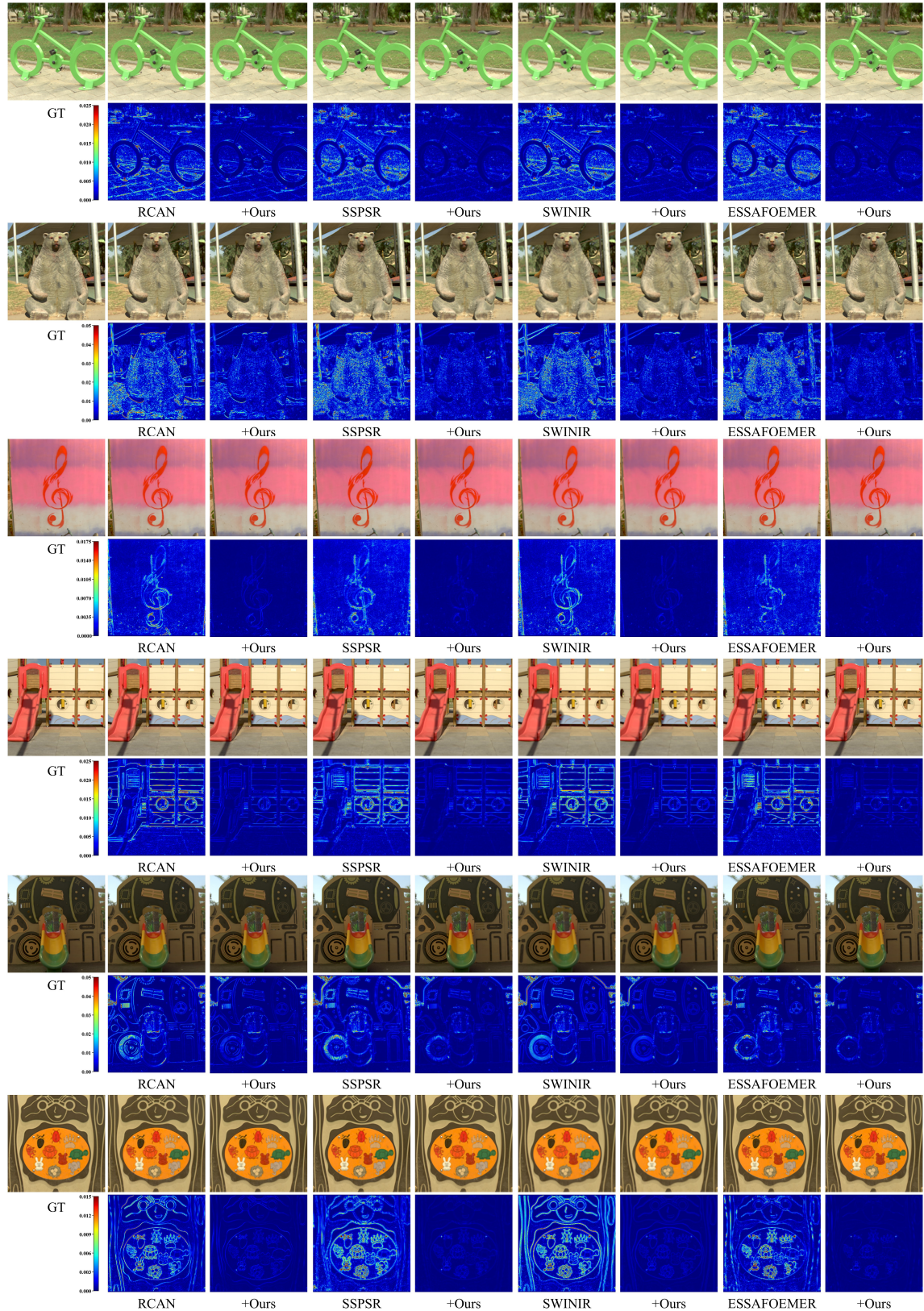


Figure 1: Representative error-map gallery on ARAD-1K at  $\times 4$ . For each scene, we show pseudo-RGB renderings and the corresponding band-averaged absolute error maps of different SR backbones, with the rectified result placed next to its baseline for direct comparison.

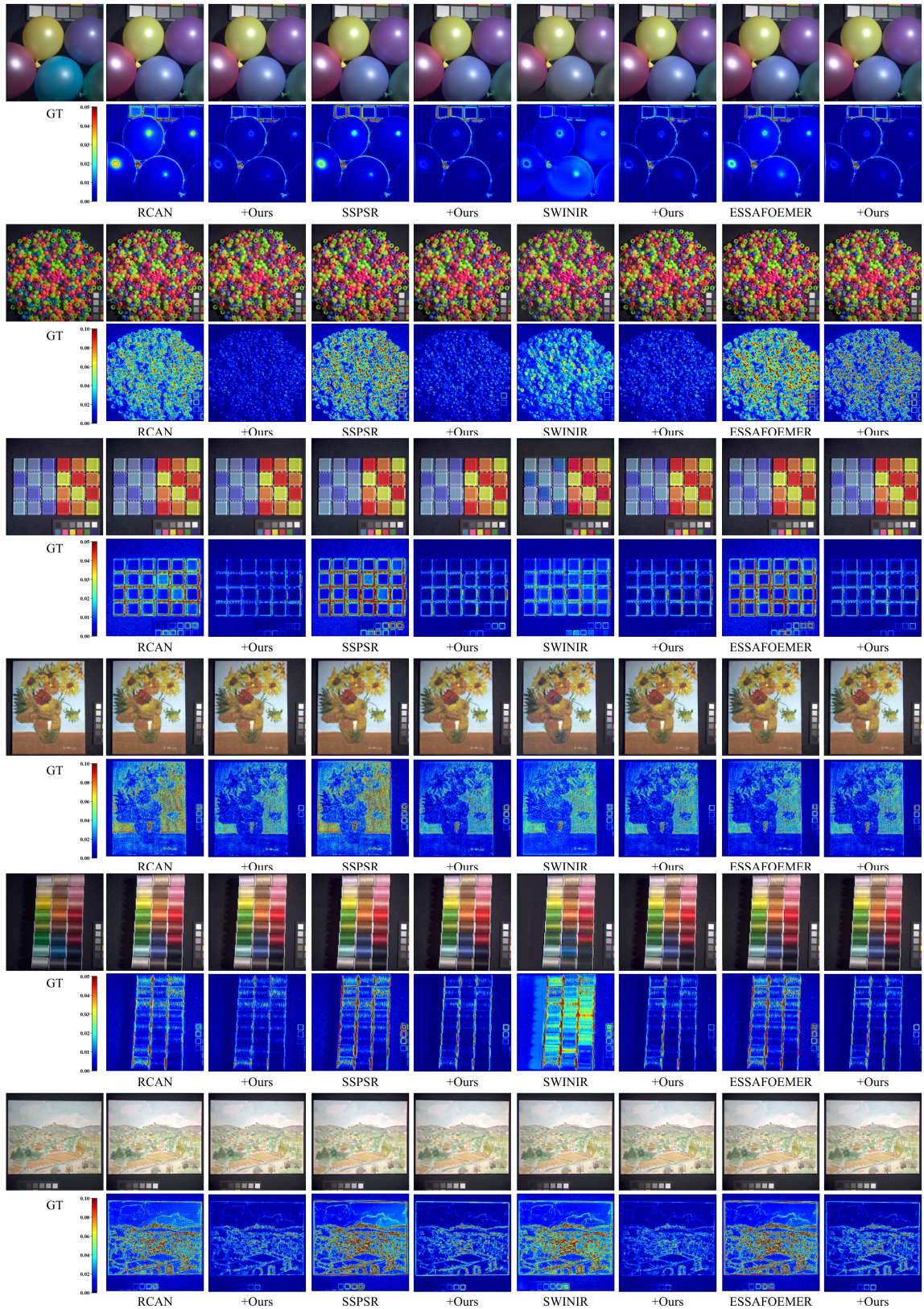


Figure 2: Representative error-map gallery on CAVE at  $\times 4$ . The visualization protocol is identical to Fig. 1.

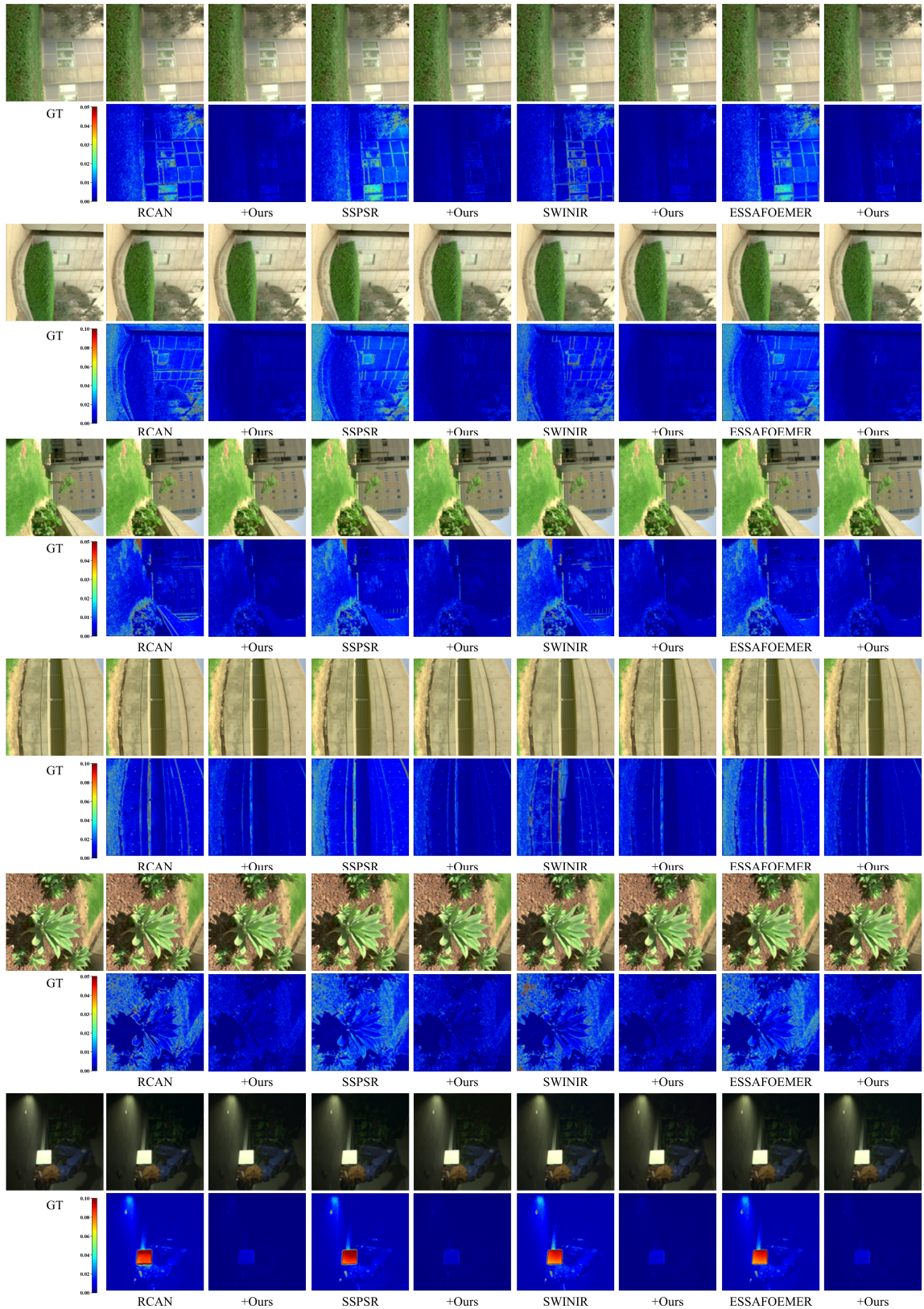


Figure 3: Representative error-map gallery on ICVL at  $\times 4$ . The visualization protocol is identical to Fig. 1.

Scale	Metric	Var.	K1	K2	B1	B2	N1	N2	N3	J1	J2
$\times 2$	mPSNR	Base	46.9930	45.2782	42.6891	39.8390	44.1997	42.8779	39.0326	41.2689	36.9781
		+Ours	47.3542	50.6912	46.3376	41.2105	46.1393	42.9718	39.2598	41.9803	37.0884
		Gain	<b>+0.3612</b>	<b>+5.4130</b>	<b>+3.6485</b>	<b>+1.3715</b>	<b>+1.9396</b>	<b>+0.0939</b>	<b>+0.2272</b>	<b>+0.7114</b>	<b>+0.1103</b>
$\times 4$	mSSIM	Base	0.9945	0.9917	0.9859	0.9742	0.9879	0.9806	0.9361	0.9754	0.9200
		+Ours	0.9949	0.9968	0.9934	0.9810	0.9892	0.9807	0.9408	0.9766	0.9270
		Gain	<b>+0.0004</b>	<b>+0.0051</b>	<b>+0.0075</b>	<b>+0.0068</b>	<b>+0.0013</b>	<b>+0.0001</b>	<b>+0.0047</b>	<b>+0.0012</b>	<b>+0.0070</b>
$\times 8$	mSAM	Base	0.6412	0.7029	0.8262	1.0349	2.2169	3.8313	7.6378	3.8589	7.6421
		+Ours	0.5743	0.5793	0.6685	0.9354	2.0748	3.7932	6.3217	3.7346	7.2463
		Gain	<b>+0.0669</b>	<b>+0.1236</b>	<b>+0.1577</b>	<b>+0.0995</b>	<b>+0.1421</b>	<b>+0.0381</b>	<b>+1.3161</b>	<b>+0.1243</b>	<b>+0.3958</b>
$\times 2$	mPSNR	Base	38.0659	37.3518	37.0133	36.4237	36.9821	36.6436	35.2832	36.3791	34.7529
		+Ours	38.7683	40.8013	40.4649	39.2507	39.2291	38.0369	35.9106	37.9000	35.3443
		Gain	<b>+0.7024</b>	<b>+3.4495</b>	<b>+3.4516</b>	<b>+2.8270</b>	<b>+2.2470</b>	<b>+1.3933</b>	<b>+0.6274</b>	<b>+1.5209</b>	<b>+0.5914</b>
$\times 4$	mSSIM	Base	0.9596	0.9531	0.9498	0.9437	0.9464	0.9395	0.9024	0.9367	0.8948
		+Ours	0.9670	0.9748	0.9731	0.9672	0.9618	0.9464	0.9086	0.9452	0.8970
		Gain	<b>+0.0074</b>	<b>+0.0217</b>	<b>+0.0233</b>	<b>+0.0235</b>	<b>+0.0154</b>	<b>+0.0069</b>	<b>+0.0062</b>	<b>+0.0085</b>	<b>+0.0022</b>
$\times 8$	mSAM	Base	1.3722	1.4583	1.4760	1.5187	2.5611	3.8740	7.0666	3.8760	7.0590
		+Ours	1.3204	1.2944	1.2709	1.2949	2.2280	3.2619	6.8138	3.2247	6.8102
		Gain	<b>+0.0518</b>	<b>+0.1639</b>	<b>+0.2051</b>	<b>+0.2238</b>	<b>+0.3331</b>	<b>+0.6121</b>	<b>+0.2528</b>	<b>+0.6513</b>	<b>+0.2488</b>
$\times 2$	mPSNR	Base	32.6296	32.3557	32.3143	32.2368	32.0617	31.8439	31.1646	31.7823	31.0966
		+Ours	33.3445	34.8300	34.8294	34.7736	34.1853	33.6229	31.9019	33.6025	31.9108
		Gain	<b>+0.7149</b>	<b>+2.4743</b>	<b>+2.5151</b>	<b>+2.5368</b>	<b>+2.1236</b>	<b>+1.7790</b>	<b>+0.7373</b>	<b>+1.8202</b>	<b>+0.8142</b>
$\times 4$	mSSIM	Base	0.8769	0.8698	0.8689	0.8672	0.8608	0.8526	0.8230	0.8518	0.8211
		+Ours	0.8968	0.9102	0.9098	0.9087	0.8953	0.8796	0.8289	0.8790	0.8265
		Gain	<b>+0.0199</b>	<b>+0.0404</b>	<b>+0.0409</b>	<b>+0.0415</b>	<b>+0.0345</b>	<b>+0.0270</b>	<b>+0.0059</b>	<b>+0.0272</b>	<b>+0.0054</b>
$\times 8$	mSAM	Base	2.3049	2.4180	2.4190	2.4220	3.0980	4.0295	6.5479	4.0262	6.5525
		+Ours	2.2712	2.1173	2.1052	2.0901	2.8654	3.5249	6.3644	3.5022	5.9158
		Gain	<b>+0.0337</b>	<b>+0.3007</b>	<b>+0.3138</b>	<b>+0.3319</b>	<b>+0.2326</b>	<b>+0.5046</b>	<b>+0.1835</b>	<b>+0.5240</b>	<b>+0.6367</b>

Table 2: Robustness to mild test-time degradation mismatch on ARAD-1K. We consider nine test-time settings grouped as kernel mismatch (K1: area downsampling; K2: an alternative bicubic implementation), blur mismatch (B1/B2: HR-space Gaussian blur with  $\sigma \in \{0.6, 1.0\}$  using  $5 \times 5$  and  $7 \times 7$  kernels before bicubic downsampling), noise mismatch (N1/N2/N3: i.i.d. Gaussian noise added in LR after downsampling with  $\sigma = n/255$  for  $n \in \{1, 2, 5\}$ ), and combined blur+noise mismatch (J1/J2:  $(\sigma, n) \in \{(0.6, 2), (1.0, 5)\}$ ). Gain is computed as (+Ours – Base) for mPSNR/mSSIM and (Base – +Ours) for mSAM.

Method	$\times 2$				$\times 4$				$\times 8$			
	mPSNR↑	mSAM↓	mSSIM↑	CC↑	mPSNR↑	mSAM↓	mSSIM↑	CC↑	mPSNR↑	mSAM↓	mSSIM↑	CC↑
Base (SwinIR)	50.4662	0.7727	0.9972	0.9990	39.5717	1.3950	0.9709	0.9902	32.5185	2.4680	0.8869	0.9551
Base + SG	46.1893	1.9059	0.9959	0.9975	38.7834	2.4512	0.9698	0.9889	32.3362	3.2638	0.8859	0.9541
Base + PCA	50.7837	0.6188	0.9972	0.9990	39.5729	1.4028	0.9709	0.9902	32.5198	2.4601	0.8869	0.9552
Base + IBP	51.0962	0.5211	0.9973	0.9992	39.5782	1.3693	0.9709	0.9902	32.5041	2.4365	0.8865	0.9548
Base + MCR	<b>51.2531</b>	<b>0.5182</b>	<b>0.9973</b>	<b>0.9992</b>	<b>40.2550</b>	<b>1.3173</b>	<b>0.9752</b>	<b>0.9912</b>	<b>33.9241</b>	<b>2.2159</b>	<b>0.8947</b>	<b>0.9675</b>
Base + Ours	51.6551	0.4842	0.9975	0.9993	40.9720	1.2819	0.9752	0.9924	34.8318	2.1164	0.9103	0.9720

Table 3: Comparison to simple spectral rectifiers on ARAD using SwinIR at  $\times 2$ ,  $\times 4$ , and  $\times 8$ . SG/PCA/IBP are applied post hoc to the fixed SwinIR output. MCR is our proposed rectification module (a component of  $SR^2$ -Net) evaluated as a standalone post hoc rectifier, while  $SR^2$ -Net is trained end-to-end.

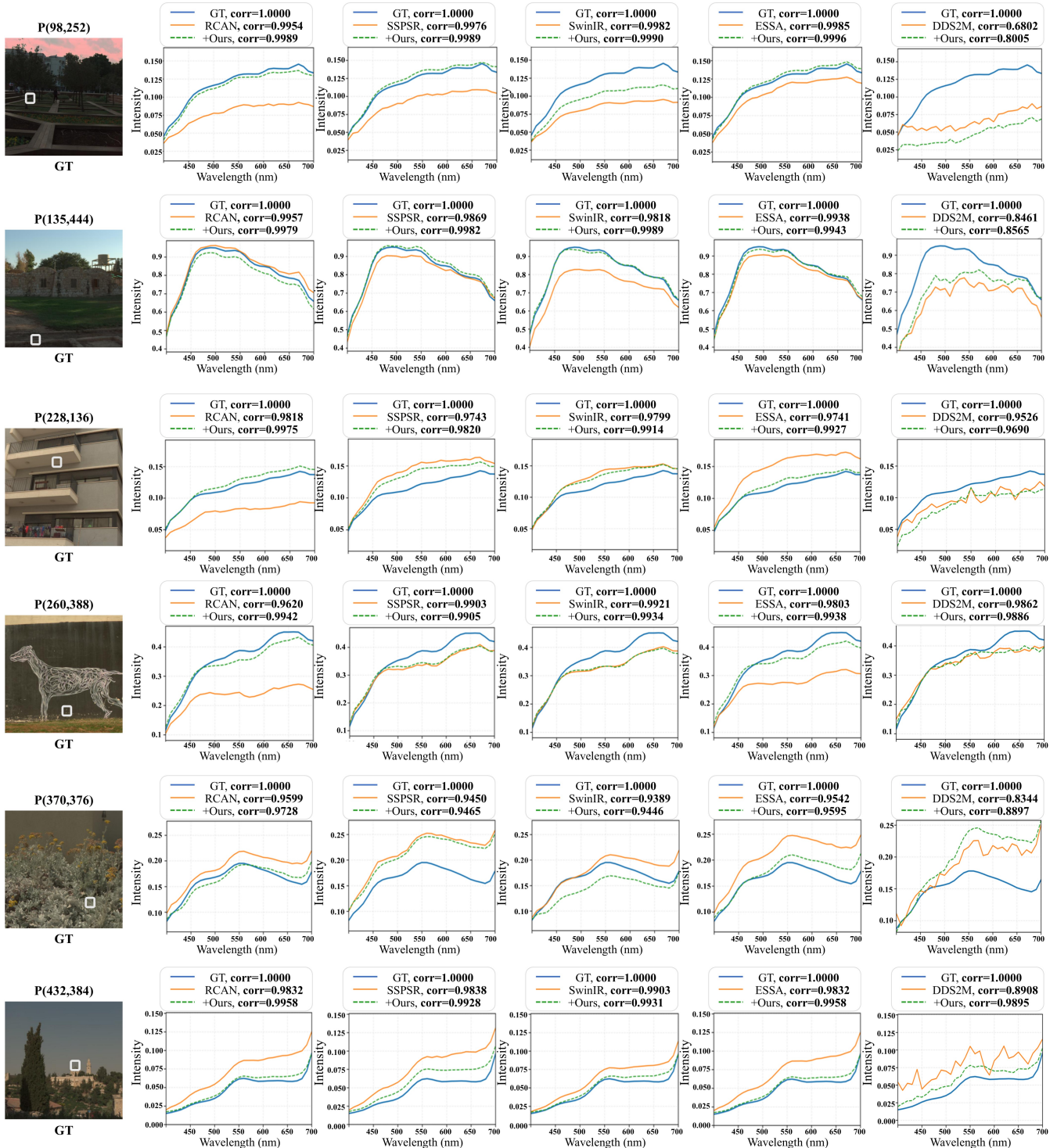


Figure 4: Additional spectral curve gallery on ARAD-1K at  $\times 4$ . Curves include CNN-, Transformer-, and diffusion-based backbones, including DDS2M.

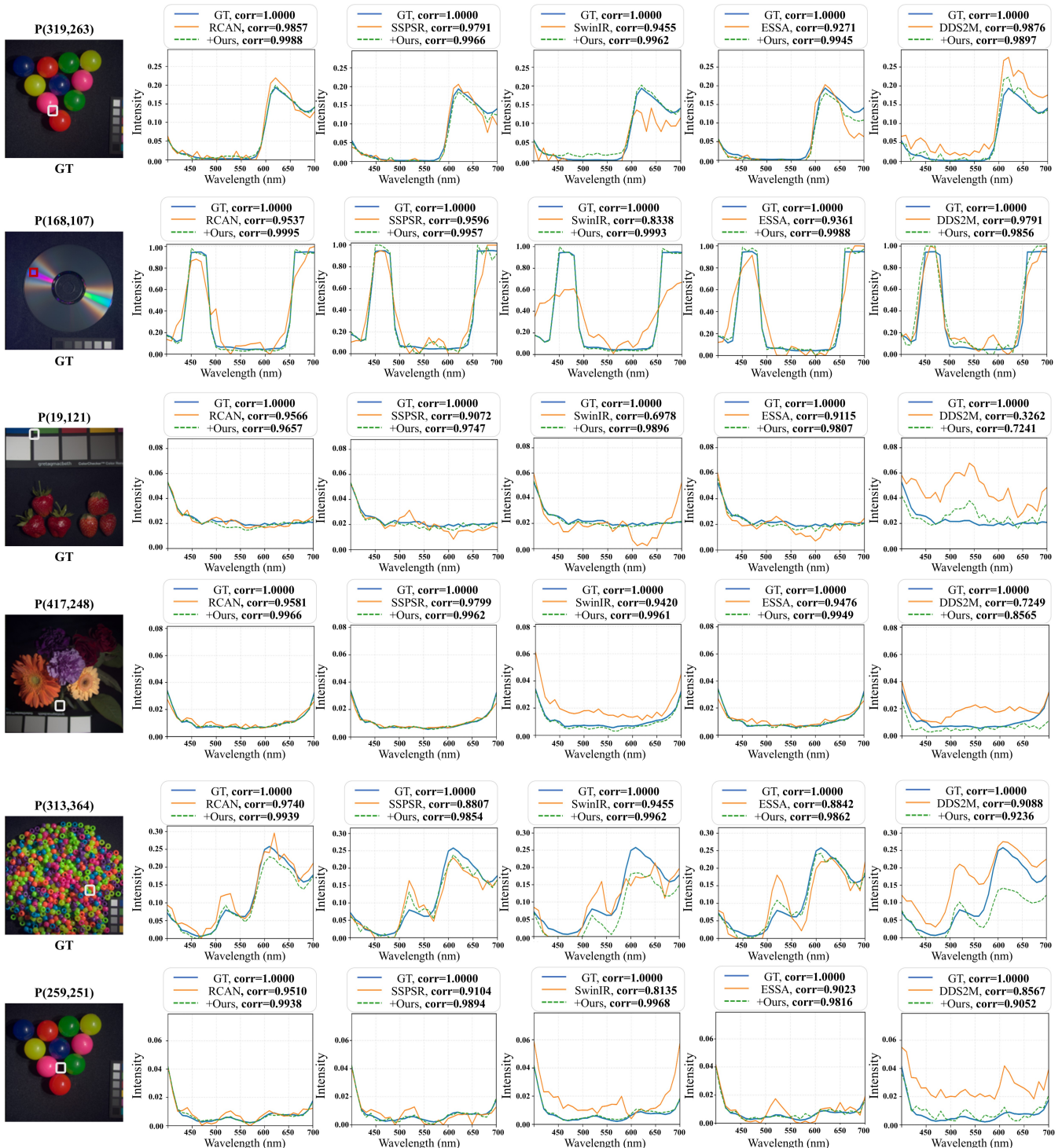


Figure 5: Additional spectral curve on CAVE at  $\times 4$ .

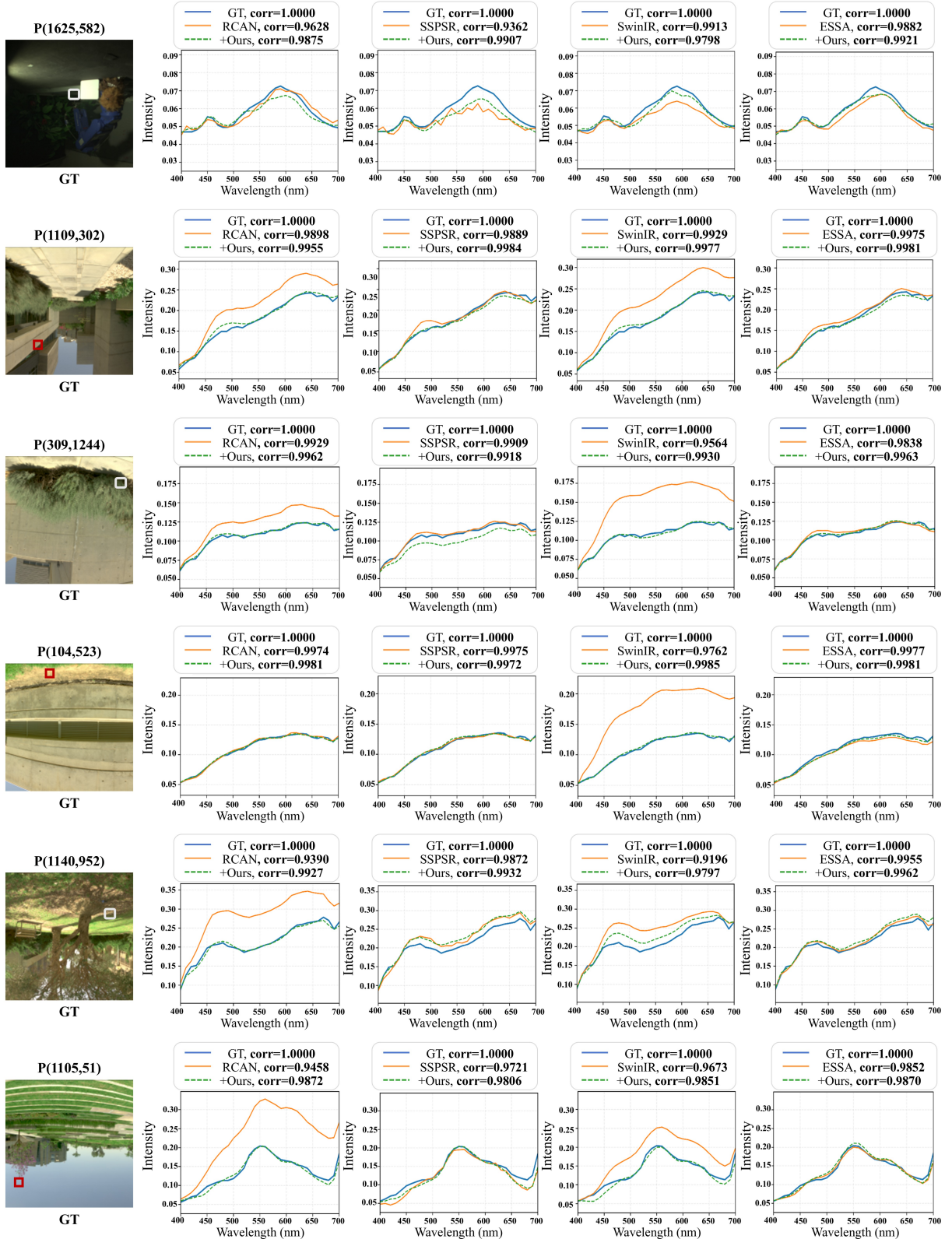


Figure 6: Additional spectral curve gallery on ICVL at  $\times 4$ .

## 2.5 Comparison to Simple Spectral Rectifiers

To address the concern that spectral rectification might be achievable by simpler low-cost alternatives, we compare *SR<sup>2</sup>-Net* against three representative post-hoc spectral rectifiers. All baselines operate on the output of a *fixed* SwinIR model and do not modify the SR backbone weights. In contrast, *SR<sup>2</sup>-Net* is trained end-to-end as a plug-and-play rectification module.

**Implementation details of SG/PCA/IBP. Savitzky–Golay smoothing (SG).** We apply a 1D Savitzky–Golay filter along the spectral dimension for each pixel independently. We use a window length  $w = 7$  and polynomial order  $p = 3$ . To avoid boundary bias, the spectrum is symmetrically padded by reflection before filtering, and then cropped back to the original length.

**PCA projection.** We fit a dataset-level PCA subspace using randomly sampled pixel spectra from the ARAD-1K training split and keep it fixed at test time. We set the rank to  $k = 8$  and use 20,000 sampled spectra in total. Given an estimated spectrum, PCA rectification is performed by projection onto the top- $k$  principal components and reconstruction back to the original spectral space.

**Iterative back-projection (IBP).** Starting from the SwinIR output, IBP refines the SR estimate by enforcing consistency with the observed LR image under an assumed degradation. We perform  $T = 10$  refinement steps with step size  $\eta = 1.0$ :

$$I_{\text{SR}}^{(t+1)} = I_{\text{SR}}^{(t)} + \eta \cdot \mathcal{U}\left(I_{\text{LR}} - \mathcal{D}\left(I_{\text{SR}}^{(t)}\right)\right), \quad (4)$$

where  $\mathcal{D}$  is the same bicubic downsampling operator used in training and  $\mathcal{U}$  is its corresponding bicubic upsampling. IBP is applied independently to each spectral band, which keeps the procedure lightweight while improving degradation consistency.

**Quantitative comparison on ARAD-1K.** Tab. 3 reports results on ARAD-1K with SwinIR as the base SR model. SG can suppress oscillations but often over-smooths informative spectral variations, leading to worse reconstruction. PCA projection imposes a low-rank spectral prior and improves spectral fidelity over SG, but its gain is limited by a fixed subspace and weak spatial adaptivity. IBP improves measurement consistency, yet it cannot directly correct cross-band structural errors from the backbone, resulting in smaller improvements in spectral metrics and MCR.

Compared with these low-cost alternatives, *SR<sup>2</sup>-Net* achieves the best overall performance across all scales, improving spatial quality and spectral fidelity while also yielding the highest MCR. This suggests that effective rectification requires more than smoothing or a global low-rank prior, and benefits from content-adaptive cross-band correction coupled with spatial structures. For clarity, we report *SR<sup>2</sup>-Net* as an additional row in Tab. 3. *SR<sup>2</sup>-Net* is trained end-to-end, whereas SG/PCA/IBP are post-hoc operations applied to a fixed SwinIR output.